Journal of Materials Chemistry A

ROYAL SOCIETY OF CHEMISTRY

PAPER

View Article Online
View Journal | View Issue

Cite this: J. Mater. Chem. A, 2020, 8, 18254

Structural characterization of a polycrystalline epitaxially-fused colloidal quantum dot superlattice by electron tomography†

Xiaolei Chu,[a] Hamed Heidari,[a] Alex Abelson,[b] Davis Unruh,[c] Chase Hansen,[c] Caroline Qian,[d] Gergely Zimanyi,[c] Matt Law*[bde] and Adam J. Moulé*[a]

Three dimensional epitaxially-fused colloidal quantum dot (QD) superlattices (epi-SLs) feature exceptional electronic coupling and spatial order and are promising systems for studying the emergence of delocalized states and mini-band charge transport in self-assembled solids. However, energy disorder arising from structural defects and aperiodicity has so far resulted in charge carrier localization and slow hopping transport. Detailed 3D structural characterization is critical for rationally improving epi-SL structural perfection to trigger the formation of mini-bands. Here, we analyze the 3D structure of a 120 × 38 nm disc-shaped region of a PbSe QD epi-SL using full-tilt high-angle annular dark-field electron tomography. The high spatial resolution of the tomographic reconstruction (0.65 nm) enables determination of the center-of-mass coordinates of all 1846 QDs in the sample as well as the size and shape of the thousands of epitaxial connections (necks) between the QDs. The tomogram reveals the detailed crystallography and internal positional disorder of the three SL grains that constitute this sample. A map of the neck network is used to quantify relationships between neck number (the number of necks each QD possesses), average neck diameter, QD location in the film, and the nearest neighbor inter-QD distance and distance distribution. We find a strong positive correlation between neck number and local spatial order, suggesting that future improvements in neck connectivity are likely to simultaneously enhance the overall structural perfection of the epi-SLs. A kinetic Monte Carlo model is employed to estimate the electron mobility of the tomography sample and assess the impact of grain boundaries on charge transport. Our electron tomography study establishes a baseline for the quantitative statistical analysis of structural defects in 3D QD epi-SLs.

Received 9th July 2020
Accepted 19th August 2020

DOI: 10.1039/d0ta06704k

rsc.li/materials-a

1 Introduction

Colloidal semiconductor quantum dots (QDs) exhibit intriguing photophysical properties relevant to next-generation solar cells,[1–4] field-effect transistors,[5,6] photodetectors[7,8] and lasers.[9,10] While improvements in QD processing, electronic performance and stability are ongoing, the use of QDs in many optoelectronic devices is limited by poor charge transport relative to bulk semiconductors. Poor transport is in part caused by energetic disorder arising from variations in QD size, spacing and other types of spatial disorder.[11–13] Epitaxially-fused PbX (X = Se, S) QD superlattices (epi-SLs) consist of PbX QDs that are arranged in a periodic lattice and epitaxially interconnected (necked or partially fused) to form a porous single crystal of "confined-but-connected" QDs. Epi-SLs promise to combine the tunable optical properties and processability of QDs with the high-efficiency band-like transport of bulk semiconductors.[14] However, charge transport studies have so far failed to demonstrate band-like transport in epi-SLs, probably because structural defects from the atomic scale to the mesoscale disrupt the SL periodicity and localize charge carriers.[15,16]

Making PbX QD epi-SLs with larger lateral grain sizes is important for reducing the density of inter-grain structural defects (*e.g.*, grain boundaries, amorphous regions, and voids), but it is the several types of intra-grain defects that conspire to degrade spatial order within the grains, destroy mini-bands, and prevent the emergence of delocalized states.[12,13,15] Intra-grain defects include variations in QD and neck size and shape, missing necks, missing QDs (vacancies), misaligned QDs (edge dislocations, screws dislocations, and zig-zag jitter), larger-scale wave-like oscillations in QD position that result from flow of the QD film on the liquid surface (meander), and

[a]Department of Chemical Engineering, University of California, Davis, USA. E-mail: amoule@ucdavis.edu

[b]Department of Materials Science and Engineering, University of California, Irvine, Irvine, CA 92697, USA. E-mail: matt.law@uci.edu

[c]Department of Physics, University of California, Davis, USA

[d]Department of Chemical and Biomolecular Engineering, University of California, Irvine, Irvine, CA 92697, USA

[e]Department of Chemistry, University of California, Irvine, Irvine, CA 92697, USA

† Electronic supplementary information (ESI) available. See DOI: 10.1039/d0ta06704k

variations in the surface coverage of ligands, ions, and traps, all of which will scatter carriers and disrupt SL periodicity to some degree. Most of these defects have been observed in 2D epi-SLs (QD monolayers), which are readily imaged by conventional transmission electron microscopy (TEM) and scanning transmission electron microscopy (STEM).[12,16–27] Transport measurements of 2D epi-SLs show that carriers are localized, and several groups have proposed that missing necks are a primary cause of carrier localization in these materials.[12,18] Furthermore, the electronic coupling of necked QDs is expected to be sensitive to neck polydispersity (length, width, atomic coherence, and faceting) and the number of nearest neighbor QDs.[12]

While 2D epi-SLs can be structurally characterized using traditional electron microscopy, imaging the internal details of 3D epi-SLs is more challenging.[22,28–30] Neck connectivity and projected neck size in 2D epi-SLs have been directly imaged by (S)TEM,[12,18,26] and the three-dimensional structure of these necks was deduced from single images by high-angle annular dark-field (HAADF) STEM atom counting reconstruction.[22] To date, structural characterization of 3D epi-SLs has been almost exclusively limited to X-ray scattering and conventional electron microscopy imaging/diffraction methods,[16,30–32] neither of which can visualize the intra-grain neck network or internal structural defects that are so important for understanding carrier delocalization in these materials. Electron tomography (ET) is a suitable tool for the near-atomistic structural characterization of 3D epi-SLs. The Vanmaekelbergh group has previously used ET to establish the basic unit cell of non-fused 3D binary[33,34] and ternary[35] QD SLs, 2D honeycomb epi-SLs,[20] and thin multilayer honeycomb epi-SLs.[36] Savitzky *et al.* reported a tomogram of a fused 3D PbS QD SL made at high pressure, but no assessment of necks or structural defects was presented.[37]

Here we present an in-depth and quantitative structural analysis of a 3D PbSe QD epi-SL using electron tomography. We show that with a full-tilt HAADF ET reconstruction of a disc-shaped epi-SL film (120 nm in diameter × 38 nm tall), we are able to achieve sufficient spatial resolution (0.65 nm) to determine the position of all 1,846 QDs and the size and shape of all necks in the sample. From the center-of-mass coordinates of the QDs, we find that the sample consists of three SL grains and assign the unit cell and in-plane crystallographic orientation of each grain as well as the 3D structure of the grain boundaries. The epi-SL grains have a distorted simple cubic structure with lattice parameters in agreement with our previous results.[31] Maps of the neck locations and diameters reveal that the sample has an average of 3.7 necks per QD (giving an overall network connectivity of 72%) and an average neck diameter of 4.1 nm (64% of the QD diameter). The three grains show similar distributions of neck number (necks per QD) but very different distributions of average neck diameter, reflecting significant inhomogeneity between the adjacent grains. We discover a weak positive correlation between neck number and diameter and a strong negative correlation between neck number and both the average and standard deviation of the nearest neighbor QD distance, indicating that QDs with more necks tend to have more ordered local environments. Kinetic Monte Carlo charge transport simulations show that the SL grain boundaries have little impact on carrier mobility because the three grains are interconnected by many necked QDs. The detailed and comprehensive understanding of various structural features gained from our statistical analysis of this relatively disordered polycrystalline sample can potentially inspire synthesis of 3D PbX QD epi-SLs of better structural perfection for realizing delocalized charge transport.

2 Experimental

2.1 Materials

Lead oxide (PbO, 99.999%), oleic acid (OA, technical grade, 90%), diphenylphosphine (DPP, 98%), 1-octadecene (ODE, 90%), ethylene glycol (EG, 99.8%, anhydrous), acetonitrile (99.99%, anhydrous), hexanes (≥99%, anhydrous), toluene (99.8%, anhydrous), (3-mercaptopropyl)trimethoxysilane (3-MPTMS, 95%), and *N*,*N*-dimethylformamide (DMF, 99.8%, anhydrous) were purchased from Sigma Aldrich and used as received. Trioctylphosphine (TOP, technical grade, >90%) and selenium (99.99%) were acquired from Fluka and mixed for 24 hours to form a 1 M TOP-Se stock solution. Ethylenediamine (EDA, >98.0%, anhydrous) was purchased from TCI and mixed with acetonitrile in a 1 : 1 volume ratio to make a 7.5 M EDA stock solution.

2.2 Quantum dot synthesis

PbSe QDs were synthesized and purified using standard air-free techniques. PbO (1.50 g), OA (5.00 g), and ODE (10.00 g) were mixed and degassed in a three-neck round-bottom flask at room temperature. The mixture was heated to 120 °C under vacuum to form dissolved $Pb(OA)_2$ and dry the solution. After 1 hour at 120 °C, the $Pb(OA)_2$ solution was heated to 180 °C under argon flow and 9.5 mL of a 1 M solution of TOP-Se containing 200 μL of DPP was rapidly injected into this hot solution. An immediate darkening of the solution was observed, and the QDs were grown for 105 seconds at ~160 °C. The reaction was quenched with a liquid nitrogen bath and injection of 10 mL of anhydrous hexanes. QD purification and SL fabrication were performed in glove boxes with <0.5 ppm O_2 content. The QDs were purified by two rounds of precipitation/redispersion using ethanol/hexane and stored as a powder in the glove box.

2.3 Substrate preparation

A single-side polished Si substrate was cleaned using 10 minutes of sonication in acetone, Millipore water, and then isopropanol, followed by drying in a stream of flowing air. The cleaned substrate was immersed in a 100 mM solution of 3-MTPMS in toluene for 1 hour to functionalize its native SiO_x surface for improved epi-SL adhesion, then rinsed with neat toluene and dried in flowing air.

2.4 Superlattice fabrication

An oleate-capped superlattice was prepared in the glovebox by drop casting 70 μL of a 4 g L^{-1} dispersion of PbSe QDs in

hexanes onto 6 mL of ethylene glycol (EG) in a Teflon well (3.5 × 5 × 1 cm). After depositing the QD solution, the well was immediately covered with a glass slide. The hexane evaporated over 30 minutes, resulting in a smooth, dry QD film floating on the EG surface. The glass slide was then removed and 0.1 mL of a 7.5 M solution of ethylenediamine in acetonitrile was slowly injected (5–10 s) into the EG under the QD film using a 500 μL Hamilton syringe. After 30 seconds of exposure to EDA, the resulting epi-SL film was stamp transferred to the Si substrate using a vacuum wand, rinsed vigorously with acetonitrile and dried under flowing N_2. The epi-SL film was then immediately immersed in a 10 mM solution of PbI_2 in DMF for 5 minutes, rinsed thoroughly with acetonitrile and dried under flowing N_2. This procedure is nearly identical to the one used in our previous report[31] and yields epi-SL films with similar SL unit cell, grain size, and homogeneity, including degree of QD necking, coverage of the substrate, and density of cracks. However, the film for this tomography study was somewhat thinner (40 nm *vs.* 50–80 nm) and have a higher density of intragrain extended defects (*e.g.*, partial twins) because it was prepared in a glove box with a higher O_2 concentration (5 ppm *vs.* <0.1 ppm).

2.5 Basic characterization

Optical absorbance measurements of QDs dispersed in TCE were performed with a PerkinElmer Lambda 950 spectrophotometer. Neat TCE served as the background for the solution measurements. Scanning electron microscopy was performed on both an FEI Magellan 400L XHR SEM operating at 10 kV and 25–50 pA and a JEOL JEM-2800 TEM (with a secondary electron detector) operated in STEM mode with a 1.0 nm probe size.

2.6 Grazing incidence small-angle X-ray scattering

GISAXS measurements were performed on Beamline 7.3.3 of the Advanced Light source (ALS) at Lawrence Berkeley National Laboratory using 10 keV monochromatic X-rays (λ = 1.24 Å) with an energy bandwidth of 1%. For GISAXS measurements, SL films were prepared on Si substrates and transported with the QD suspensions to the ALS under nitrogen to minimize air exposure prior to measurement. However, measurements were performed in air. A Dectris Pilatus 2M detector with a pixel size of 0.172 × 0.172 mm and 1475 × 1679 pixels was used to record the 2D scattering patterns. A silver behenate standard was used to determine the sample-to-detector distance and beam center. Exposure times ranged from 0.2 to 30 s. The grazing angle of incidence was varied from 0.2° to 0.3°. Manual pattern fitting was performed using the IndexGIXS software package provided by Detlef Smilgies of the Cornell High Energy Synchrotron Source. The critical angles of the films were fit empirically (0.195° for the oleate-capped SLs and 0.21° for the epi-SLs) to capture the breadth of the Yoneda band.

2.7 Tomography needle sample preparation

An area of the epi-SL film suitable for FIB milling was located by SEM and tagged with a Pt fiducial marker deposited by electron-beam induced deposition (EBID) in an FEI Quanta 3D FEG DualBeam microscope. The sample was then coated with 50 nm of carbon using the pulse plasma mode of a Leica ACE200 evaporator and returned to the DualBeam for FIB milling, lift-out, and final needle preparation. Prior to milling, a ~200 nm Pt capping layer was deposited onto the carbon-coated sample by EBID, followed by an additional ~2000 nm of Pt deposited by ion beam induced deposition (IBID). The carbon layer serves primarily to enhance STEM imaging contrast by separating the epi-SL layer from the high-Z protective Pt capping layer. The area of interest was then FIB milled into a wedge shape (10 μm × 6 μm × 2 μm), lifted-out with an OmniProbe 400 nanomanipulator, ion welded to the tip of a sample holder for needle tomography samples (Single Point Tip, Hummingbird Scientific), and FIB milled again into a ~130 nm diameter needle (Fig. S2†). Milling was performed in several stages. The wedge was first milled into a pillar shape (1 μm diameter) using a 0.3 nA ion beam at 30 keV accelerating voltage, then thinned to a ~200 nm diameter needle using 50 pA at 16 keV. Finally, a 5 minute ion beam shower (25 pA at 5 keV) was employed to sharpen the needle to ~130 nm and remove surface damage. The finished needle contained a disc-shaped epi-SL layer (38 nm tall × 128 nm in diameter) for tomographic analysis.

2.8 HAADF-STEM electron tomography

The needle sample was mounted on the rotation axis of a Hummingbird Scientific single-tilt tomography holder (1000 Series) and imaged in a double aberration corrected JEOL JEM-ARM 300F TEM operated at 300 keV in STEM mode (~25 mrad semi-convergence angle). Two series of images were acquired, with HAADF and bright-field data recorded simultaneously (2k × 2k images) at each tilt angle. The first series consisted of 145 HAADF images spanning tilt angles over −78° to 67° in 1° steps. The sample was then removed from the microscope, manually rotated on the sample holder by 86°, and re-imaged from −68° to 78° in 2° steps (resulting in 73 additional images). All 2D and 3D image processing was conducted in MATLAB unless otherwise noted. The two tilt-series were then merged using cross-correlation comparison (Fig. S4†). The merged tilt-series include 181 images covering tilt angles from 0° to 226°. The image stack was then aligned vertically (along the rotation axis) by iteratively shifting the images to maximize the value of the 2D normalized cross-correlation function between adjacent images in the stack. Pixels outside of the epi-SL film were excluded from this cross-correlation calculation in order to maximize the quality of the vertical image alignment. Horizontal alignment of the images (normal to the rotation axis) was accomplished by converting each image to a 1D intensity profile and shifting the images to maximize the match between the 1D curves. The aligned image stack was then processed through two iterations of a Wiener image filter to remove noise. Tomographic reconstruction was carried out on the aligned and denoised tilt-series using 200 iterations of the simultaneous iterative reconstruction technique (SIRT) in the ASTRA toolbox.[38,39] The raw reconstructed volume consisted of 2048 × 2048 × 700 voxels with edge lengths of 1 Å. The spatial resolution of this

reconstruction was evaluated by the Fourier shell correlation (FSC) method to be 6.5 Å (Fig. S5†).

The raw reconstruction was processed in two different ways. For analysis of the QD necks, the reconstruction was simply smoothed by a nonlinear anisotropic diffusion filter. Image processing for analysis of the QD positions was more involved. The raw tomogram was first filtered with a morphological 3D top-hat filter to minimize reconstruction intensity attenuation and enhance contrast. A top-hat filter was used to retain edge contrast instead of the more common Fourier filter[40] because Fourier filtering would erroneously remove necks between QDs and other important structural features present in the raw tomogram. To better emphasize the QD positions, the filtered tomogram was convolved with a spherical 6.0 nm diameter QD kernel with a homogeneous intensity profile to obtain a 3D map of normalized cross-correlation (NCC) coefficients indicating the center of mass of each QD in the sample. Use of the 6.0 nm QD template is justified by the analysis of the average QD size and polydispersity from conventional dark-field STEM images (pixel size of 0.2 nm) of a different area of the same sample (Fig. S6†). Prior to data analysis, the outer 6 nm of the cylinder-shaped tomogram was digitally removed to exclude QDs near the surface of the sample that were potentially deformed by the FIB milling process. To automate the measurement of neck dimensions, a script was written that defines a plane normal to each inter-QD axis and slides this plane along the axis to locate the minimum neck area. The neck diameter was then determined as the diameter of a circle of the same area.

2.9 Mobility simulation

Mobility simulations were performed utilizing the Hierarchical Nanoparticle Transport Simulator (HiNTS) kinetic Monte Carlo code, developed by some of us previously.[41,42] HiNTS simulates transport by developing several modeling layers and then integrating them into a hierarchical scheme. After the energetics of the individual QDs is computed by *ab initio* methods, the QD-to-QD transitions of the charges are described by the following two mechanisms:

(1) Miller–Abrahams single phonon-assisted hopping between nearest neighbor QDs:

$$\Gamma_{i\to j}=\begin{cases}\nu g_{ij}\beta_{ij}\exp\left(\dfrac{-\Delta E_{ij}}{k_{\mathrm{b}}T}\right) & \text{if } \Delta E_{ij}>0,\\ \nu g_{ij}\beta_{ij} & \text{if } \Delta E_{ij}\le 0\end{cases} \quad (1)$$

where ν is a suitably chosen prefactor, g_{ij} is the product of the initial density of states on QD_i and the final density of states on QD_j, β_{ij} is the tunneling amplitude evaluated using the WKB approximation as $\beta_{ij}=\exp\left(-2\Delta x\sqrt{\dfrac{-m^*(E_i+E_j)}{\hbar^2}}\right)$, where Δx is the minimal surface separation of the QDs, m^* is the effective mass of electrons in the barrier, and E_i and E_j are the energy levels of QD_i and QD_j. Here, the tunneling energetic barrier is treated as the average of the initial and final state of the hooping.[59] ΔE_{ij} is the total energy difference associated with an electron transitioning from QD_i to QD_j: $\Delta E_{\mathrm{ij}}=\Delta E_{ij}^{\mathrm{band}}+\Delta E_{ij}^{\mathrm{charging}}+\Delta E_{ij}^{\mathrm{voltage}}$, where $\Delta E_{ij}^{\mathrm{band}}$ is calculated using the one-electron band energies of the QDs determined by *ab initio* methods,[43] $\Delta E_{ij}^{\mathrm{charging}}$ is calculated using the charging energies of the QDs as determined by a hybrid empirical-perturbative method,[44] and $\Delta E_{ij}^{\mathrm{voltage}}$ is the energy difference due to the applied voltage. In general, the QD–QD hopping can be nearest neighbor or variable range hopping. Either hopping process can involve an elastic reorganization of the QD atoms, or processes other than Miller–Abrahams, such as that described by Marcus theory. Finally, the long-range part of the Coulomb interaction may or may not be included. Of the eight possible combinations, for example,[45] we investigated the intriguing process of variable range hopping with long-range Coulomb interactions and the Marcus reorganization process. HiNTS is capable of accommodating any of these eight combinations. We chose the simplest Miller–Abrahams process because both variable range hopping and Marcus processes have been shown to become important only at low temperatures, whereas our experiments were performed at room temperature. Indeed, experiments on QD lattices regularly report the standard activated, Miller–Abrahams temperature dependence around room temperature.[46]

(2) Tunneling through the neck of epitaxially-fused QDs:

$$\Gamma_{i\to j}=\begin{cases}\dfrac{2\pi}{\hbar}|t|^2 g_{ij}\exp\left(\dfrac{-\Delta E_{ij}}{k_{\mathrm{b}}T}\right) & \text{if } \Delta E_{ij}>\mathrm{OE},\\ \dfrac{2\pi}{\hbar}|t|^2 g_{ij} & \text{if } \Delta E_{ij}\le \mathrm{OE}\end{cases} \quad (2)$$

where $|t|$ is the QD–QD tunneling matrix element, and OE is an overlap energy. This transition channel represents that when a neck is formed between two QDs, their electronic states overlap and therefore hybridize. This hybridization induces a perturbation of the energy levels of the individual QDs, which we model by an overlap energy OE that is proportional to the neck diameter. The electronic states of those pairs of QDs whose energy level difference is less than OE: $\Delta E_{\mathrm{ij}}\le \mathrm{OE}$, hybridize to such a degree that they support a metallic QD_i-to-QD_j transition instead of a hopping one, paving the way toward the formation of a mini-band. The tunneling matrix element $|t|$ depends on the wavefunction overlap between the necked QDs. For its calculation, we adopt the approximation of Fu *et al.*:[47]

$$|t|=\frac{9\hbar^2 n\rho^3}{m^* d^2} \quad (3)$$

where n is the average electron volume density of the two quantum dots, ρ is the neck radius, m^* is the effective electron mass, and d is the average QD diameter. HiNTS simulates nearest neighbor transitions and interactions; it does not include transitions to and interaction with farther neighbors.

On the next HiNTS modeling layer, a QD epi-SL is constructed. Simulations were performed on three types of epi-SL samples. First, the replica of the tomography sample was generated using the experimentally determined center-of-mass coordinates, QD diameters, and neck map of all three grains. Since the circular shape and uneven periphery of the tomography sample would make it harder to set up controlled transport simulations, QDs at the periphery of the sample were

removed to reduce the simulation volume to the well-defined central cuboid of the tomography sample. To develop a comparative analysis of the transport of this tomography sample, we next generated two ensembles of over a thousand samples each to form a comparison basis. The first ensemble consisted of monocrystalline epi-SLs with the lattice parameters and neck statistics of grain I of the tomogram. The second ensemble consisted of bicrystalline epi-SLs with the same lattice parameters and neck statistics of grain I, but bisected by a plane of missing necks normal to the transport direction to create a necking grain boundary. The QDs in the latter two types of samples were assigned a diameter and lattice displacement vector according to the experimentally-determined Gaussian distributions.

Electron transport was simulated by first randomly placing electrons on QDs to fill the samples with a predetermined density of electrons. Based on our previous work, we chose the electron density to be 0.5 electrons per QD, remaining far from commensuration to avoid Coulomb blockade effects.[41] A small voltage of 1 mV was then applied across electrical contacts on opposite sides of each sample to induce electron transport. Periodic boundary conditions were used. Throughout the simulation, we checked and ensured that the current–voltage characteristic stayed in the linear regime. Finally, the mobility was determined according to the following equation:

$$\mu = \frac{\text{electrons collected at drain electrode} \times l}{\text{total number of electrons} \times t \times E} \quad (4)$$

where l is the length of simulation box normal to the electrodes, t is the simulation time, and E is the applied electric field. The transport across every sample in both ensembles was simulated.

3 Results and discussion

3.1 SL unit cell and disorder

Oleate-capped PbSe QDs with a diameter of 6.4 ± 0.3 nm were used to fabricate a 3D polycrystalline epi-SL film *via* self-assembly and ligand exchange on a liquid ethylene glycol substrate (Fig. 1a and Methods).[16,17,48,49] After triggering epitaxial fusion of the QDs with EDA, the epi-SL film was stamped onto a silicon substrate, immersed in a solution of PbI_2 to remove additional oleate ligands, and milled by focused ion beam (FIB) into a 128 nm diameter disc embedded in a nanoscale needle for full-tilt electron tomography studies (Fig. 1a). Scanning electron microscopy (SEM) images of the epi-

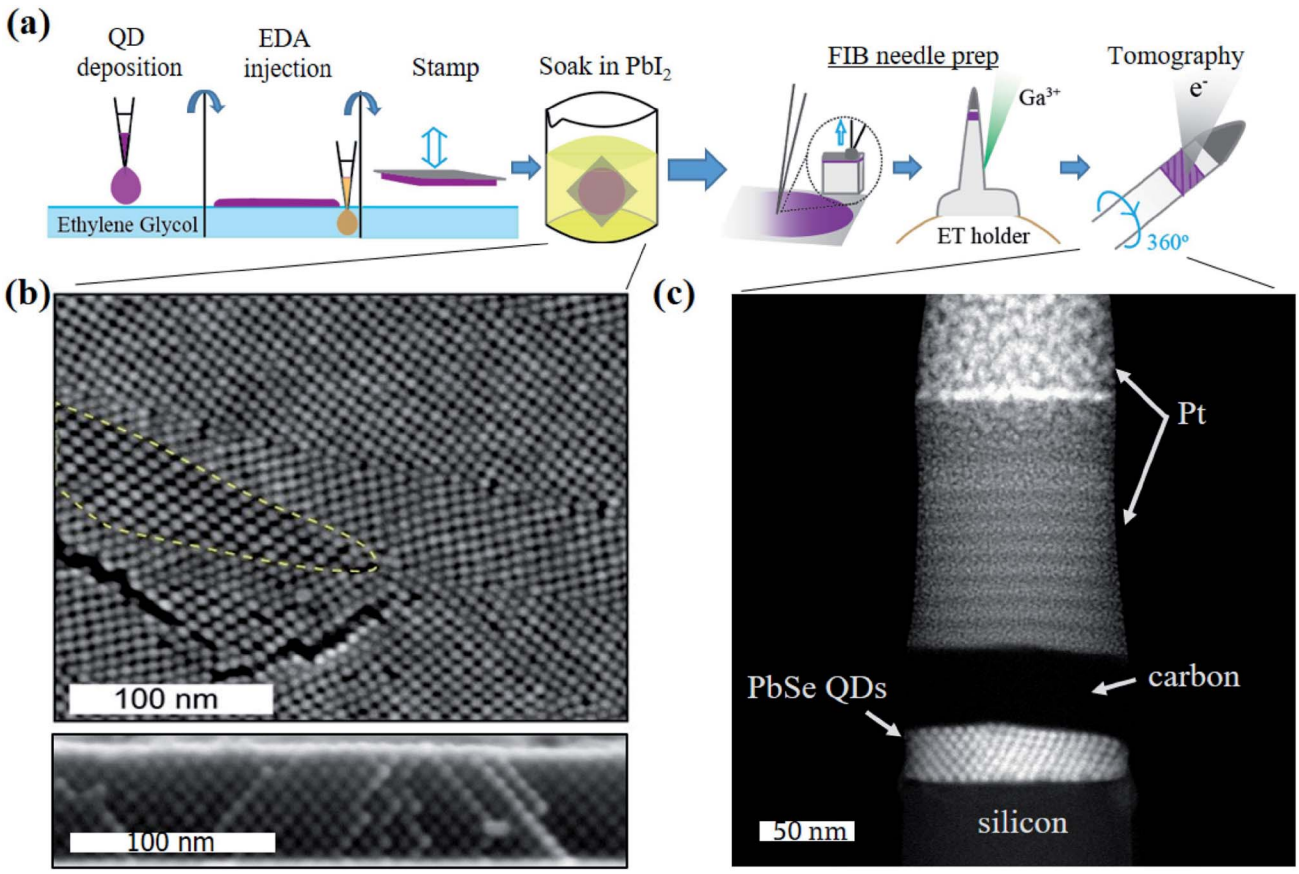

Fig. 1 Fabrication of the PbSe QD epi-superlattice tomography sample. (a) Sample fabrication. (b) Plan-view and cross-section SEM images of a different region of the epi-SL film. The film is a polycrystalline SL with SL grains of two different in-plane orientations, previously assigned to the $(100)_{SL}$ and $(01\bar{1})_{SL}$ projections of a distorted simple cubic SL.[31] Most of the SL grains in this image have a $(100)_{SL}$ orientation. The dashed yellow line encircles a $(01\bar{1})_{SL}$-oriented grain. Scale bars are 100 nm. (c) HAADF-STEM image of the needle-shaped tomography sample with disc-shaped epi-SL layer and all layers labeled. Scale bar is 50 nm.

SL film and the finished tomography needle are presented in Fig. 1b and c, respectively. An optical extinction spectrum of the QDs in solution and additional details about the preparation of the tomography sample are provided in the ESI (Fig. S1 and S2†).

We acquired a ±113° single-axis tilt-series of 181 images of the sample using high-angle annular dark-field scanning transmission electron microscopy (HAADF-STEM) in a double aberration-corrected microscope (see Methods and Fig. S3 and S4†). Tomographic reconstruction of the sample was accomplished using the SIRT algorithm after careful image alignment and noise filtering. The final tomogram (Fig. 2a and Movie S1†) has a spatial resolution of 6.5 Å (~1 unit cell of PbSe) as determined by the Fourier shell correlation (FSC) method (Fig. S5†). This resolution is sufficient to unambiguously identify the center of mass (CoM) coordinates of all 1,846 QDs in the sample volume, as illustrated in Fig. 2e and f.

The CoM data were used to determine the size, shape, crystallographic orientation, and lattice parameters of the constituent SL grains as well as the presence of inter-grain defects (grain boundaries, amorphous domains, voids) and intra-grain defects. Visual inspection of Fig. 2 shows that the sample is seven QD layers thick and consists of three cylindrical sector-shaped (pie slice) SL grains that meet at a grain boundary triple junction near the center of the tomogram (dashed lines in Fig. 2a–d). While it is possible to assign the SL grain crystallography *a priori* from the CoM coordinates, we utilized the known unit cell of similarly-prepared PbSe QD epi-SLs[31] (distorted simple cubic with $a = 6.6 \pm 0.2$ nm and $\alpha = 99 \pm 2°$; Fig. S7†) to help interpret the tomogram. Grain I has a square-like lattice of QDs in each QD layer parallel to the substrate, so it

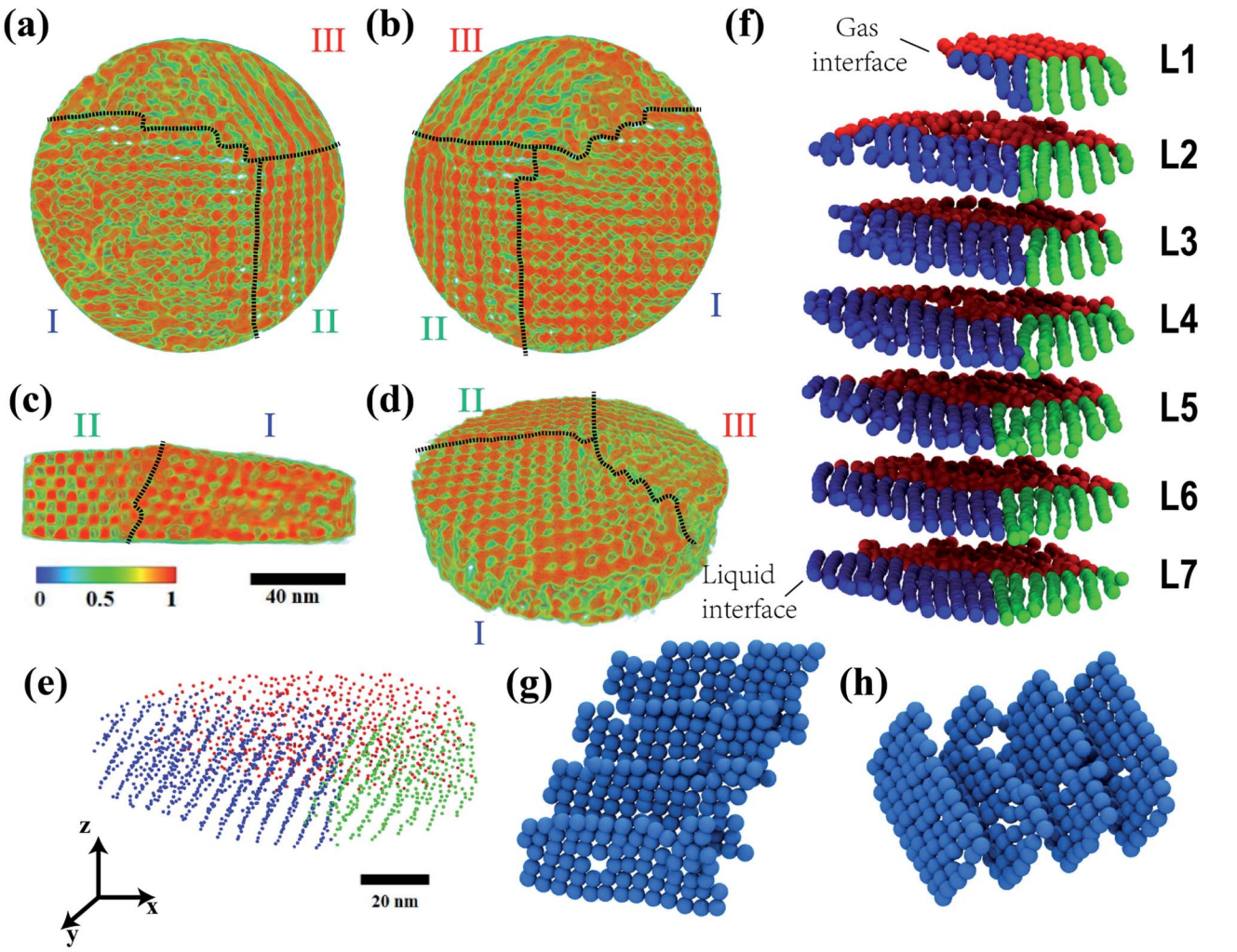

Fig. 2 The epi-SL tomogram and QD positions. (a) Top, (b) bottom, (c) cross-section, and (d) perspective views of the tomogram of the epi-SL film. The color scale denotes the normalized electron density in units of e^- per nm^3. Dashed lines represent grain boundaries between the three SL grains (labeled grain I, II, and III). The scale bar is 40 nm. (e) Perspective image of the center of mass coordinates of all QDs in the sample. Each QD is represented by a sphere with a diameter of 1 nm (for ease of viewing). The QDs are color coded according to their location in grain I (blue), grain II (green), or grain III (red). The scale bar is 20 nm. (f) Exploded view of the seven QD layers of the sample to illustrate the internal structure of the epi-SL film. Each QD is represented by a 6 nm diameter sphere (Fig. S6†). Layer 1 (L1) is the top layer of the originally floating film (at the QD/gas interface), while layer 7 (L7) is the bottom layer of the film (at the liquid/QD interface). The QDs are color coded according to panel (e). (g and h) Representative monolayers in grain I separated along direction *x* and *y*, representing SL lattice planes of (g) $(100)_{SL}$ and (h) $(010)_{SL}$.

is assigned as a $(100)_{SL}$-oriented SL grain, which is the most common grain orientation in this sample (see Fig. 1b). Grains II and III have 1D chains of QDs in each layer parallel to the substrate, with an average QD spacing of a along the chains and $\sqrt{2}a$ between the chains. This arrangement is consistent with the $(01\bar{1})_{SL}$ projection of the distorted simple cubic SL unit cell, so grains II and III are assigned as $(01\bar{1})_{SL}$-oriented SL grains (again, see Fig. 1b). Grains II and III intersect at a planar coherent twin boundary indexed as 39°[001],(010) (most easily seen in Fig. 2a and b). Between grains I and II, it is harder to define a grain boundary interface as we observe in Fig. 2c a relatively smooth change in the $[001]_{SL}$ lattice vector from grain II on the left side to grain I on the right side. A possible mechanism for such an inter-grain orientational transition is proposed in Fig. S8† involving a small rotation and a subsequent glide of the $(100)_{SL}$ plane. Grains I and III meet at a highly-corrugated boundary. All three grain boundaries are normal or nearly normal to the substrate and span the entire thickness of the QD film (Fig. 2f). SEM images of similar grain boundaries are presented in Fig. S9.† In Fig. 2g and h, we show representative separated layers in grain I along two other lattice vectors showing QD vacancies from different perspectives. The randomness in the QD positional order is shown to occur in all directions. We also note that there is no significant difference in the vacancy rate for layers normal to different lattice vectors. Several slice views of the tomogram taken at different angles are shown in Fig. S10† emphasizing the orientational differences between SL unit cells of grain I and II and also how the lateral and vertical monolayers are connected through necks. See Movies S2 and S3† for additional continuous slices of this sample.

We determined the lattice parameters of grains I and II by compiling nearest-neighbor QD distances and bond angles from the CoM data (see Fig. S11† for labeling conventions). Grain III was excluded from this analysis due to its poor spatial order. Histograms of the QD distances and angles (Fig. S12 and S13†) show Gaussian distributions with average and standard deviation values summarized in Table 1. The lattice constants of grains I and II are in good agreement with the unit cell parameters of similar epi-SL films derived from ensemble GISAXS measurements,[31] so we conclude that these epi-SLs have essentially the same crystal structure, validating the recent GISAXS results. However, grains I and II also exhibit broad distributions of distances and angles indicative of a relatively large amount of positional disorder, as is apparent from Fig. 2. The spatial order of this sample is likely limited by the structural disorder of the original oleate-capped SL, the presence of several nearby grain boundaries, variability in QD neck number and diameter (*vide infra*), and (possibly) mechanical strain caused by sample preparation. Two additional aspects of the data are noteworthy. First, while grains I and II have very similar triclinic unit cells, they differ slightly in their β angle (Table 1). Such grain-to-grain variability is expected in polycrystalline SLs due to local differences in grain nucleation and growth, especially when the SL grains are small and experience non-uniform stress. Electron tomography is one of the few techniques capable of detecting such minute structural differences between individual QD SL grains. Second, grain I is slightly compressed along the film normal with a smaller average lattice spacing in c direction shown in Table 1. This is commonly seen for nanocrystal films prepared by solvent evaporation.[50–53]

Table 1 Lattice constants of SL grains I and II as determined from statistical analysis of the tomogram. GISAXS data is from ref. 31

Grain	a/nm	b/nm	c/nm	α	β	γ
I	6.4 ± 0.6	6.4 ± 0.6	5.9 ± 0.7	102 ± 8°	95 ± 7°	96 ± 7°
II	6.3 ± 0.6	6.5 ± 0.6	6.2 ± 0.7	103 ± 9°	107 ± 5°	97 ± 7°
GISAXS		6.6 ± 0.2			99 ± 2°	

3.2 Characterization of neck disorder

In addition to the positions of the QDs, the tomogram provides rich information about the crystalline connections (necks) between the QDs. Previous TEM studies have shown that the QDs in these SLs are epitaxially fused across their {100} facets.[22,27,30,32,54,55] The epitaxial necks likely dictate the strength and uniformity of electronic coupling within the epi-SLs,[11] so mapping the location and size of the necks is essential for understanding and optimizing the electronic properties of these materials. Electron tomography can directly visualize the necks and map the 3D neck network inside each SL grain. Fig. 3a shows a slice of the tomogram through the middle of L4 with the necks between the QDs clearly visible. We implemented an automated program to measure the cross-sectional area of every neck in the sample and assign each an effective diameter (Fig. S14†). In our approach, any connection with an area smaller than the tomogram spatial resolution (0.43 nm^2, or about one PbSe unit cell) was considered to be absent (a "missing neck"). An example of a missing neck is shown in Fig. 3d.

Heat maps of the average neck diameter and the total number of necks for each QD in L4 are presented in Fig. 3b and c. Maps for all seven layers of the sample are compiled in Fig. S16 and S17.† The 1846 QDs in the sample have a maximum of 4865 possible epitaxial necks (considering the six {100} facets of each QD and sample edge effects, vacancies, and voids). We observe a total of 3471 necks, giving an overall network connectivity of 72%, well above the bond percolation threshold (p_c) of 25% for simple cubic lattices.[56] This estimate of neck connectivity is conservative because, as mentioned above, any neck smaller than the tomogram resolution (≤3 Pb atoms wide) is not counted by our algorithm. Overall, the average number of necks per QD is 3.7 and the average neck diameter is 4.1 nm (64% of the QD diameter). Table 2 summarizes the neck statistics for the sample.

Fig. 3e and f show histograms of neck number and diameter for the three epi-SL grains in this sample. The neck number for all three grains follows a beta distribution (solid curves) with a peak at 3.5–4 necks per QD. Grain I has the largest fraction of QDs with high connectivity (five and six necks), while grain II has the largest fraction of QDs with intermediate connectivity (four necks) and the smallest fraction of QDs with low

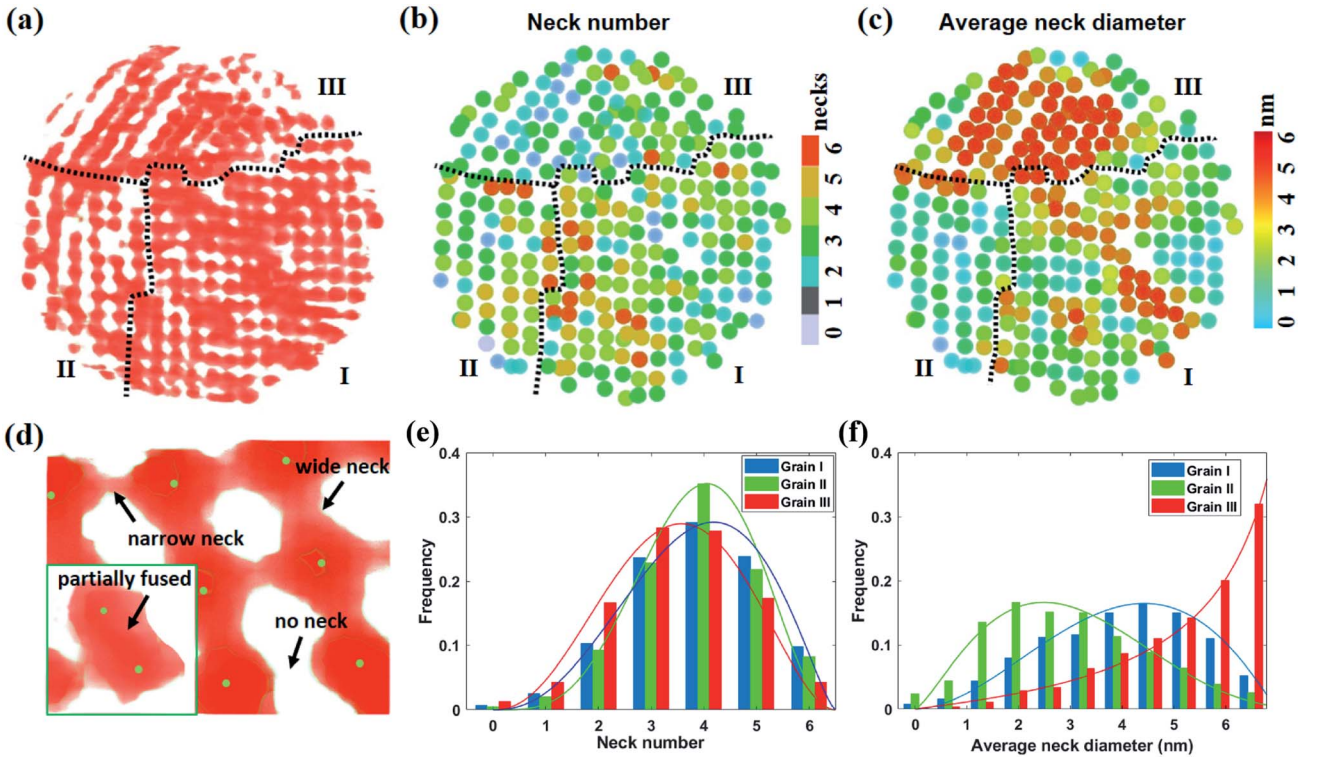

Fig. 3 Analysis of the QD necks. (a) A slice of the tomogram through the middle of L4, showing in-plane necks between the QDs. (b) Heat map of the total number of necks for each QD in L4. The color scale is labeled. (c) Heat map of the average neck diameter for each QD in L4, including both in-plane and out-of-plane necks. The color scale is labeled. (d) Magnified isosurface views of two regions of the sample to illustrate typical neck polydispersity (narrow, wide, and missing necks) and a highly-fused pair of QDs (inset). The green dots denote the CoM of each QD. (e) Histograms of neck number for all QDs in grains I, II and III (inclusive of L1–L7, not just L4). The solid curves are fitted beta distributions. (f) Corresponding histograms of average neck diameter. Fitting beta distributions are shown as solid curves. See Fig. S15† for histograms of the diameter of every neck in each grain.

Table 2 Neck statistics

Parameter	Grain I	Grain II	Grain III	Total
Number of QDs	903	389	554	1846
QD number density (cm^{-3}) × 10^{-18}	3.9	3.7	3.5	3.7 (3.5[a])
Space filling fraction	0.53	0.51	0.48	0.51
Possible necks	2343	1028	1494	4865
Observed necks	1760	774	959	3493
Connectivity	75%	75%	64%	72%
Average number of necks	3.8	4.0	3.4	3.7
Average neck diameter (nm)	4.0	3.5	5.0	4.1

[a] From ref. 31.

connectivity (three or fewer necks). Overall, grains I and II are quite similar with respect to neck number. In contrast, grain III has much poorer neck connectivity than grains I and II, with the smallest fraction of high-connectivity QDs and the largest fraction of low-connectivity QDs. Grain III is also dominated by QDs with very large neck diameters (see the J-shaped distribution in Fig. 3f). The low neck number and large fraction of heavily-fused QDs contribute to the poor spatial order of grain III. The average neck diameters of grains I and II also follow a beta distribution and are similarly polydisperse. These two beta distributions (grain I: $\alpha = 2.90$, $\beta = 2.25$; grain II: $\alpha = 2.10$, $\beta = 3.18$) are approximately mirror images of each other (Fig. 3f). Grain I has a larger fraction of thicker necks (>4 nm) while grain II has a larger fraction of thinner necks (<4 nm). The reason for these differences in neck diameter and number in adjacent epi-SL grains is unclear, but probably related to variability in the spatial order of the parent oleate-capped SL and the kinetics of the epi-SL phase transition. We attempted to determine a correlation between neck number and diameter to measure whether the number of necks on each QD determined the neck thickness. ESI Fig. S18a† shows this correlation for the full sample and for each of the grains, indicating little correlation between the number of necks and the neck thickness for each QD, but also clearly showing that the average neck thickness is consistent throughout the grain regardless of the number of necks. Understanding the origin of such differences between grains will require systematic study of many tomograms to establish statistical relationships.

We also investigated possible trends in the necking conditions that depend on the position of the layer within the SL. Fig. S18b and c† plot the average neck number and diameter for each of the seven QD layers of the film. We find that the neck number is essentially constant in the middle five QD layers of

grains I and II, while the neck number is significantly lower in grain III. However, there is a reduced neck number in L1 (the top of the film) for grains I–III and L7 (the bottom of the film) for grains II and III, despite taking into account edge effects. We conclude that the top and bottom monolayers of the epi-SL tend to have fewer necks per QD. For all three grains, the neck diameter is smaller in L1 and L7 and increases in the middle of the film (Fig. 4c). Interestingly, while neck number and neck thickness are not in general correlated, the number and thickness of necks is lower at the QD/liquid and QD/gas interfaces, which suggests that out-of-plane forces from adjacent layers are important for necking formation and order. One might also expect to observe a monotonic decrease in neck number and diameter along the film normal due to ligand (glycoxide and oleate) concentration gradients since the ligands diffuse into the SL from the QD/liquid interface. Our neck diameter profile suggests that no such concentration gradients exist in this sample, in agreement with recent infrared spectroscopy measurements showing homogeneous ligand exchange in films of similar thickness.[31]

We also explored the relationship between neck number and the local spatial order of the epi-SL. In the ideal averaged epi-SL unit cell (Fig. S7†), each QD is necked to six nearest neighbors (NNs) located at a common center-to-center distance and fixed lattice angles. In contrast, QDs in real epi-SLs have distributions of neck number, NN distance, and lattice angles. These distributions provide a measure of the local (nanoscale) spatial disorder of the QD array. We reasoned that the distribution of NN distances and lattice angles should depend strongly on neck number because necks can form over only a narrow range of QD positions. Thus, QDs with high (low) connectivity should have more (less) ordered local environments. To assess the impact of neck number on local spatial order, we compiled histograms of the nearest neighbor distance (d_{NN}) as a function of neck number for all of the QDs in grains I and II (Fig. 4a). Grain III was again excluded from analysis due to its poor order. We find that as neck number increases, the average NN distance ($\bar{d}_{NN}$) and standard deviation of the distance (σ_d) decrease in a linear fashion. As Fig. 4b and c shows, d_{NN} decreases from ~7.2 nm for QDs with one neck to ~6.0 nm for QDs with six necks, while σ_d decreases from 1.1 nm to 0.5 nm (a 55% reduction). Although this simple metric is limited to NNs and neglects the propagation of disorder across longer length scales,[30] it demonstrates the importance of neck connectivity to the structural order of QD epi-SLs: high neck number is associated with high local spatial order. Future tomograms of more perfect monocrystalline samples will be used to map, understand, and ultimately minimize the multiscale spatial disorder of these QD solids.

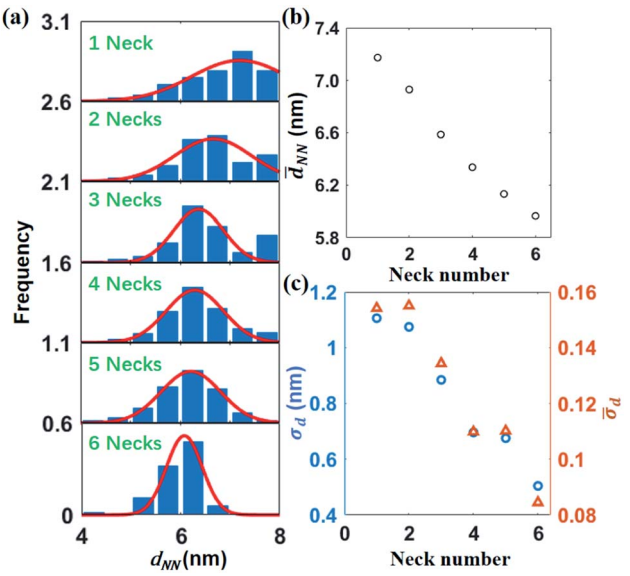

Fig. 4 Correlation of neck number with nearest neighbor QD positional disorder. (a) Histograms of NN distance (d_{NN}) at each neck number for all of the QDs in grains I and II. Overlaid red curves are Gaussian fits. (b) Plot of the average NN distance ($\bar{d}_{NN}$) *versus* neck number. (c) Plot of the standard deviation of the NN distance (σ_d) and the normalized standard deviation of the NN distance ($\bar{\sigma}_d = \sigma_d/\bar{d}_{NN}$) *versus* neck number. $\bar{\sigma}_d$ is a measure of the local disorder that is independent of differences in unit cell size.

3.3 Charge transport simulation

Charge transport in the epi-SL tomography sample was simulated with the HiNTS code. As described in the Methods section, the simulated tomography sample was generated using the QD CoM coordinates and neck network of the experimental tomogram and trimmed into a cuboid shape with electrodes on opposite faces (Fig. 5a). In this geometry, electrons must cross the grain boundary between grains I and II, or I and III, to traverse the sample. The tomogram shows that grains I, II, and III are connected by many necks across these grain boundaries. The mobility of the tomography sample was found to be ~4.6 $cm^2\ V^{-1}\ s^{-1}$ (Fig. 5d).

To probe the relative importance of the necking *versus* the conventional SL grain boundaries, and the disorder for the electron transport across the tomography sample, mobility simulations were also performed on the two ensembles of its monocrystalline and bicrystalline analogues. First, we compared the mobility of the tomography sample to that of the ensemble of monocrystalline (single-grain) epi-SLs with the same lattice parameters and neck statistics as grain I (Fig. 5b). Relative to the monocrystalline samples, the tomography sample has three grains separated by SL grain boundaries, but these grain boundaries are bridged by a large number of inter-QD necks. In spite of these differences, the mobility of the tomography sample remains typical of the mobility distribution of the ensemble of monocrystalline epi-SLs, as shown in the upper panel of Fig. 5d. Next, we also calculated the carrier mobilities of the ensemble of bicrystalline (double-grain) epi-SLs, generated by removing a bisecting plane of necks from the monocrystalline samples (Fig. 5c). Electrons can move across this "necking grain boundary" only by hopping, which is significantly slower than direct tunneling through necks. We find that the computed average mobility decreases by ~25% as a consequence of splitting the neck network in two (lower panel of Fig. 5d). The introduction of the necking grain boundary

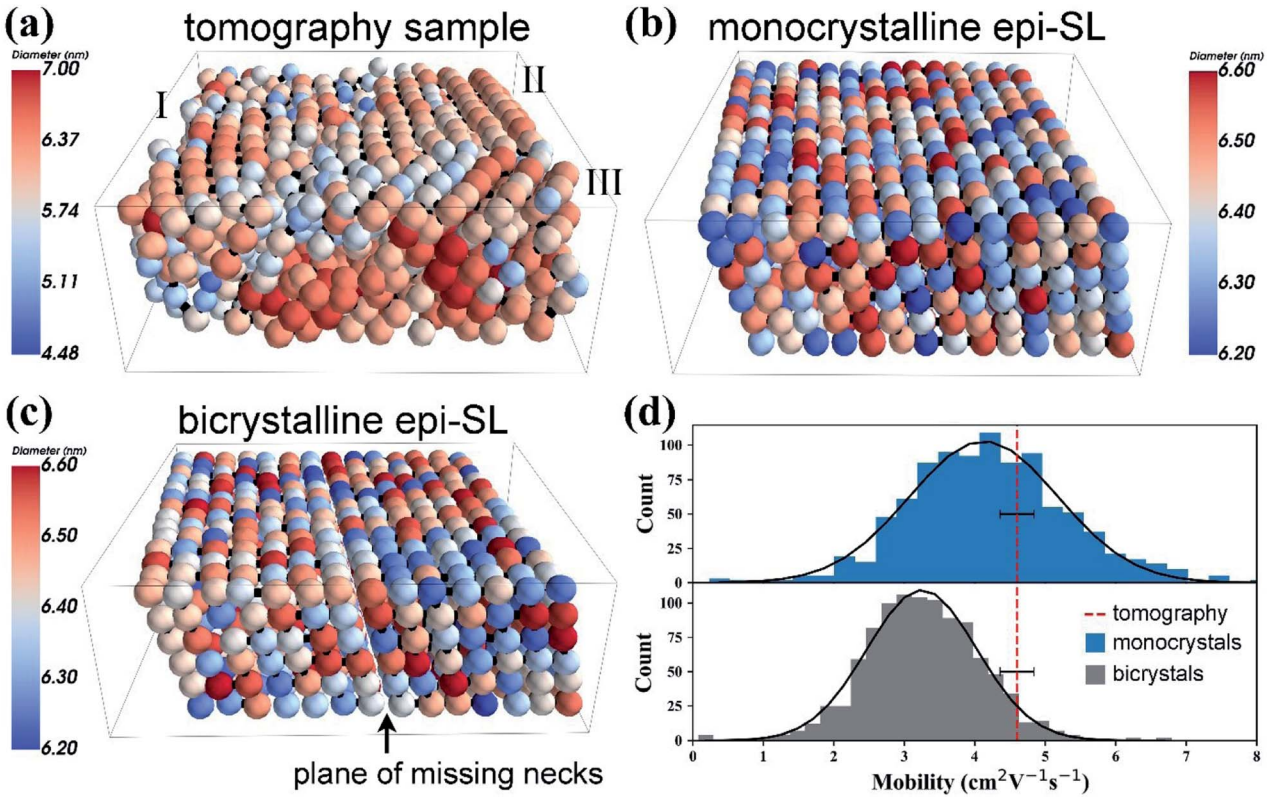

Fig. 5 Transport simulation results. (a–c) Perspective views of the three types of simulated samples. (a) The tomography sample (trimmed from a disc into a cuboid). Grains I, II, and III are labeled. (b) A monocrystalline epi-SL. (c) A bicrystalline epi-SL. The monocrystalline and bicrystalline epi-SLs were generated using the lattice parameters, QD size distribution, QD positional disorder and neck statistics of grain I. The bicrystalline samples are bisected by a plane of missing necks (a necking grain boundary), which limits transport across this plane to hopping. Virtual electrical contacts are placed at the left and right sides of each sample. All simulation boxes are approximately 92 × 92 × 39 nm. (d) Comparison of the calculated electron mobility of the tomography sample (dashed red line), monocrystalline epi-SLs (blue bars) and bicrystalline epi-SLs (gray bars). The horizontal error bar represents the error in the mobility estimate for the tomography sample. Overlaid black curves are Gaussian fits of the histograms. The mobility for the monocrystalline and bicrystalline samples is 4.25 ± 1.25 $cm^2 V^{-1} s^{-1}$ and 3.28 ± 0.8 $cm^2 V^{-1} s^{-1}$, respectively.

makes the mobility of the tomography sample largely inconsistent with the bicrystalline mobility distribution.

The most natural explanation of these results is that the mobility in these strongly disordered epi-SLs is primarily determined by transport across the inter-QD neck network, while SL grain boundaries impact the mobility only to a limited degree as long as inter-QD necks continue to connect the SL grains across the SL grain boundary with a reasonable density. The tomography sample falls into this category: this explains why its mobility is consistent with the mobility distribution of the monocrystalline samples. In contrast, when a sample is bisected with a neck grain boundary, so that the two grains cease to be connected by inter-QD necks, electrons are forced to thermally hop across no-neck boundaries rather than tunnel through necks, thereby reducing the mobility by a substantial amount. Our analysis suggests that the formation of necks between QDs across conventional SL grain boundaries is an efficient way to substantially increase carrier transport across those grain boundaries. Strategies to enhance the mobility in SLs were already discussed in earlier works, wherein the importance of reducing the disorder of SLs to form mini-bands was emphasized.[57] A key message of the present paper is that the mobility of QD SLs can also be substantially improved by forming sample-spanning neck networks. In a single-grain sample, charge transport should be improved by regulating intra-grain necking conditions such as decreasing neck size dispersity and increasing connectivity. This is particularly true for QD SL based photovoltaics, where the charge carriers are collected along the through-plane (film normal) direction of the multilayer instead of in-plane direction. We did observe a higher through-plane connectivity of QDs in grain I that might suggest anisotropic necking conditions in a 3D epi-SL film. However, further investigations should be conducted to look into the effect of the degree of such structural anisotropy on the mobility, and will more rely on structural statistics from single-grain tomography samples, which is beyond the scope of this paper.

4 Conclusion

We analyzed a full-tilt electron tomographic reconstruction of a disc-shaped region of a 3D epitaxially-connected PbSe QD SL film. This tomogram provides (i) sufficiently high spatial resolution (0.65 nm) to accurately determine the position and size/

shape of the QDs and their necks and (ii) sufficiently large volume (4.3×10^5 nm^3) to enable meaningful statistical analysis of structural disorder in the sample. We showed that the sample consists of three SL grains and assigned the unit cell and in-plane crystallographic orientation of each grain as well as the structure of the three grain boundaries. Maps of the neck locations and diameters revealed that the sample has an average of 3.7 necks per QD (overall network connectivity of 72%) and an average neck diameter of 4.1 nm (64% of the QD diameter). In testing correlations between neck number, neck diameter, inter-QD distance, and QD location in the film, we discovered a strong association between neck number and both the average and standard deviation of the nearest neighbor QD distance, demonstrating that QDs with more necks tend to have more ordered local environments. Achieving more complete, uniform necking will require fabrication of more perfect oleate-capped SLs and greater control of the kinetics of the phase transition from the oleate-capped SL to the epi-SL.

We also simulated the combined nearest-neighbor hopping/tunneling transport in this SL film. Simulations of monocrystalline and bicrystalline analogues showed that SL grain boundaries have limited impact on the electron mobility as long as the grains remain interconnected by necked QDs that form percolating neck networks. An encouraging message of this result is that high mobilities can still be achieved in QD SLs even if they have a high density of grain boundaries, and thus small grain sizes, by increasing the QD attachment density, or neck connectivity, across the SL grain boundaries. To complete the picture, it is natural to expect that once the neck networks connect most of the QDs of the epi-SL to the point that carriers delocalize into mini-bands, further mobility enhancements can be achieved by reducing the density of conventional SL grain boundaries as well.

Our study sets a baseline for the quantitative structural characterization of 3D QD epi-SLs. Looking forward, electron tomography will likely be an important tool for elucidating processing/structure/property relationships and guiding the fabrication of increasingly perfect 3D epi-SLs. Higher-quality epi-SLs will in turn encourage more in-depth analysis of the tomograms, particularly with regard to disorder across length scales longer than those emphasized in this paper.[30] Finally, we note that improving the tomogram resolution by a factor of two would allow visualization of QD facets and atomic-scale defects such as edge dislocations,[58] thereby providing a comprehensive near-atomistic picture of the 3D structure of these mesoscale QD films.

Conflicts of interest

There are no conflicts of interest to declare.

Acknowledgements

This work was supported by the UC Office of the President under the UC Laboratory Fees Research Program Collaborative Research and Training Award LFR-17-477148. We thank Jian-Guo Zheng for assistance with FIB sample preparation and Toshihiro Aoki with help with TEM. Electron microscopy was performed at the user facilities of the UC Irvine Materials Research Institute (IMRI). The GISAXS measurements used resources of the Advanced Light Source at Lawrence Berkeley National Laboratory.

Notes and references

1 A. G. Pattantyus-Abraham, I. J. Kramer, A. R. Barkhouse, X. Wang, G. Konstantatos, R. Debnath, L. Levina, I. Raabe, M. K. Nazeeruddin, M. Gratzel and E. Sargent, *ACS Nano*, 2010, **4**, 3374–3380.
2 E. H. Sargent, *Nat. Photonics*, 2012, **6**, 133.
3 G. H. Carey, A. L. Abdelhady, Z. Ning, S. M. Thon, O. M. Bakr and E. H. Sargent, *Chem. Rev.*, 2015, **115**, 12732–12763.
4 Y. Kim, F. Che, J. W. Jo, J. Choi, F. P. García de Arquer, O. Voznyy, B. Sun, J. Kim, M.-J. Choi, R. Quintero-Bermudez, *et al.*, *Adv. Mater.*, 2019, 1805580.
5 C. R. Kagan, E. Lifshitz, E. H. Sargent and D. V. Talapin, *Science*, 2016, **353**, aac5523.
6 S. J. Oh, Z. Wang, N. E. Berry, J.-H. Choi, T. Zhao, E. A. Gaulding, T. Paik, Y. Lai, C. B. Murray and C. R. Kagan, *Nano Lett.*, 2014, **14**, 6210–6216.
7 G. Konstantatos and E. H. Sargent, *Infrared Phys. Technol.*, 2011, **54**, 278–282.
8 M. M. Ackerman, X. Tang and P. Guyot-Sionnest, *ACS Nano*, 2018, **12**, 7264–7271.
9 C. Dang, J. Lee, C. Breen, J. S. Steckel, S. Coe-Sullivan and A. Nurmikko, *Nat. Nanotechnol.*, 2012, **7**, 335.
10 Y. Chen, J. Herrnsdorf, B. Guilhabert, Y. Zhang, I. M. Watson, E. Gu, N. Laurand and M. D. Dawson, *Opt. Express*, 2011, **19**, 2996–3003.
11 Y. Liu, M. Gibbs, J. Puthussery, S. Gaik, R. Ihly, H. W. Hillhouse and M. Law, *Nano Lett.*, 2010, **10**, 1960–1969.
12 K. Whitham, J. Yang, B. H. Savitzky, L. F. Kourkoutis, F. Wise and T. Hanrath, *Nat. Mater.*, 2016, **15**, 557.
13 P. Guyot-Sionnest, *J. Phys. Chem. Lett.*, 2012, **3**, 1169–1175.
14 I. Moreels, K. Lambert, D. Smeets, D. De Muynck, T. Nollet, J. C. Martins, F. Vanhaecke, A. Vantomme, C. Delerue, G. Allan, *et al.*, *ACS Nano*, 2009, **3**, 3023–3030.
15 C. R. Kagan and C. B. Murray, *Nat. Nanotechnol.*, 2015, **10**, 1013.
16 W. J. Baumgardner, K. Whitham and T. Hanrath, *Nano Lett.*, 2013, **13**, 3225–3231.
17 W. H. Evers, B. Goris, S. Bals, M. Casavola, J. De Graaf, R. Van Roij, M. Dijkstra and D. Vanmaekelbergh, *Nano Lett.*, 2012, **13**, 2317–2323.
18 W. H. Evers, J. M. Schins, M. Aerts, A. Kulkarni, P. Capiod, M. Berthe, B. Grandidier, C. Delerue, H. S. Van Der Zant, C. Van Overbeek, *et al.*, *Nat. Commun.*, 2015, **6**, 8195.
19 C. S. Sandeep, J. M. Azpiroz, W. H. Evers, S. C. Boehme, I. Moreels, S. Kinge, L. D. Siebbeles, I. Infante and A. J. Houtepen, *ACS Nano*, 2014, **8**, 11499–11511.
20 M. P. Boneschanscher, W. H. Evers, J. J. Geuchies, T. Altantzis, B. Goris, F. T. Rabouw, S. Van Rossum, H. S. van der Zant, L. D. Siebbeles, G. Van Tendeloo, *et al.*, *Science*, 2014, **344**, 1377–1380.
21 M. Zhao, F. Yang, C. Liang, D. Wang, D. Ding, J. Lv, J. Zhang, W. Hu, C. Lu and Z. Tang, *Adv. Funct. Mater.*, 2016, **26**, 5182–5188.

22 J. J. Geuchies, C. Van Overbeek, W. H. Evers, B. Goris, A. De Backer, A. P. Gantapara, F. T. Rabouw, J. Hilhorst, J. L. Peters, O. Konovalov, *et al.*, *Nat. Mater.*, 2016, **15**, 1248.
23 W. Walravens, J. De Roo, E. Drijvers, S. Ten Brinck, E. Solano, J. Dendooven, C. Detavernier, I. Infante and Z. Hens, *ACS Nano*, 2016, **10**, 6861–6870.
24 M. Zhao, D. Ding, F. Yang, D. Wang, J. Lv, W. Hu, C. Lu and Z. Tang, *Nano Res.*, 2017, **10**, 1249–1257.
25 B. E. Treml, B. H. Savitzky, A. M. Tirmzi, J. C. DaSilva, L. F. Kourkoutis and T. Hanrath, *ACS Appl. Mater. Interfaces*, 2017, **9**, 13500–13507.
26 D. M. Balazs, B. M. Matysiak, J. Momand, A. G. Shulga, M. Ibáñez, M. V. Kovalenko, B. J. Kooi and M. A. Loi, *Adv. Mater.*, 2018, **30**, 1802265.
27 C. Van Overbeek, J. L. Peters, S. A. Van Rossum, M. Smits, M. A. Van Huis and D. Vanmaekelbergh, *J. Phys. Chem. C*, 2018, **122**, 12464–12473.
28 B. T. Diroll, N. J. Greybush, C. R. Kagan and C. B. Murray, *Chem. Mater.*, 2015, **27**, 2998–3008.
29 D. Altamura, V. Holý, D. Siliqi, I. C. Lekshmi, C. Nobile, G. Maruccio, P. D. Cozzoli, L. Fan, F. Gozzo and C. Giannini, *Cryst. Growth Des.*, 2012, **12**, 5505–5512.
30 B. H. Savitzky, R. Hovden, K. Whitham, J. Yang, F. Wise, T. Hanrath and L. F. Kourkoutis, *Nano Lett.*, 2016, **16**, 5714–5718.
31 A. Abelson, C. Qian, T. Salk, Z. Luan, K. Fu, J.-G. Zheng, J. L. Wardini and M. Law, *Nat. Mater.*, 2020, **19**, 49–55.
32 K. Whitham and T. Hanrath, *J. Phys. Chem. Lett.*, 2017, **8**, 2623–2628.
33 H. Friedrich, C. J. Gommes, K. Overgaag, J. D. Meeldijk, W. H. Evers, B. d. Nijs, M. P. Boneschanscher, P. E. de Jongh, A. J. Verkleij, K. P. de Jong, *et al.*, *Nano Lett.*, 2009, **9**, 2719–2724.
34 M. P. Boneschanscher, W. H. Evers, W. Qi, J. D. Meeldijk, M. Dijkstra and D. Vanmaekelbergh, *Nano Lett.*, 2013, **13**, 1312–1316.
35 W. H. Evers, H. Friedrich, L. Filion, M. Dijkstra and D. Vanmaekelbergh, *Angew. Chem., Int. Ed.*, 2009, **48**, 9655–9657.
36 J. L. Peters, T. Altantzis, I. Lobato, M. A. Jazi, C. Van Overbeek, S. Bals, D. Vanmaekelbergh and S. B. Sinai, *Chem. Mater.*, 2018, **30**, 4831–4837.
37 B. H. Savitzky, K. Whitham, K. Bian, R. Hovden, T. Hanrath and L. F. Kourkoutis, *Microsc. Microanal.*, 2014, **20**, 542–543.
38 J. Trampert and J.-J. Leveque, *J. Geophys. Res.: Solid Earth*, 1990, **95**, 12553–12559.
39 W. van Aarle, W. J. Palenstijn, J. De Beenhouwer, T. Altantzis, S. Bals, K. J. Batenburg and J. Sijbers, *Ultramicroscopy*, 2015, **157**, 35–47.
40 C.-C. Chen, C. Zhu, E. R. White, C.-Y. Chiu, M. Scott, B. Regan, L. D. Marks, Y. Huang and J. Miao, *Nature*, 2013, **496**, 74.
41 D. Unruh, C. Hansen, A. Camjanyi, J. Bobadilla, M. Rozenberg and G. T. Zimanyi, 2019, arXiv.org, e-Print Arch., Condens. Matter.
42 L. Qu, M. Vörös and G. T. Zimanyi, *Sci. Rep.*, 2017, **7**, 7071.
43 I. Kang and F. W. Wise, *J. Opt. Soc. Am. B*, 1997, **14**, 1632–1646.
44 C. J. Delerue and M. Lannoo, *Nanostructures: Theory and Modeling*, Springer Science & Business Media, 2013.
45 A. J. Houtepen, D. Kockmann and D. Vanmaekelbergh, *Nano Lett.*, 2008, **8**, 3516–3520.
46 D. Yu, C. Wang, B. L. Wehrenberg and P. Guyot-Sionnest, *Phys. Rev. Lett.*, 2004, **92**, 216802.
47 H. Fu, K. V. Reich and B. I. Shklovskii, *Phys. Rev. B*, 2016, **93**, 125430.
48 A. Dong, J. Chen, P. M. Vora, J. M. Kikkawa and C. B. Murray, *Nature*, 2010, **466**, 474.
49 A. Dong, Y. Jiao and D. J. Milliron, *ACS Nano*, 2013, **7**, 10978–10984.
50 M. C. Weidman, D.-M. Smilgies and W. A. Tisdale, *Nat. Mater.*, 2016, **15**, 775.
51 T. Hanrath, J. J. Choi and D.-M. Smilgies, *ACS Nano*, 2009, **3**, 2975–2988.
52 D. K. Smith, B. Goodfellow, D.-M. Smilgies and B. A. Korgel, *J. Am. Chem. Soc.*, 2009, **131**, 3281–3290.
53 D. Dunphy, H. Fan, X. Li, J. Wang and C. J. Brinker, *Langmuir*, 2008, **24**, 10575–10578.
54 A. R. McCray, B. H. Savitzky, K. Whitham, T. Hanrath and L. F. Kourkoutis, *ACS Nano*, 2019, **13**, 11460–11468.
55 Y. Wang, X. Peng, A. Abelson, P. Xiao, C. Qian, L. Yu, C. Ophus, P. Ercius, L.-W. Wang, M. Law, *et al.*, *Sci. Adv.*, 2019, **5**, eaaw5623.
56 J. Wang, Z. Zhou, W. Zhang, T. M. Garoni and Y. Deng, *Phys. Rev. E: Stat., Nonlinear, Soft Matter Phys.*, 2013, **87**, 052107.
57 Y. Liu, J. Tolentino, M. Gibbs, R. Ihly, C. L. Perkins, Y. Liu, N. Crawford, J. C. Hemminger and M. Law, *Nano Lett.*, 2013, **13**, 1578–1587.
58 W. Walravens, E. Solano, F. Geenen, J. Dendooven, O. Gorobtsov, A. Tadjine, N. Mahmoud, P. P. Ding, J. P. Ruff, A. Singer, *et al.*, *ACS Nano*, 2019, **13**, 12774–12786.
59 R. E. Chandler, A. J. Houtepen, J. Nelson and D. Vanmaekelbergh, *Phys. Rev. B*, 2007, **75**(8), 085325.